nanomaterials

MDPI

Article

MOF-Derived Co Nanoparticles Catalyst Assisted by F- and N-Doped Carbon Quantum Dots for Oxygen Reduction

Yuqi Ma †, Ki-Wook Sung † and Hyo-Jin Ahn *

Department of Materials Science and Engineering, Seoul National University of Science and Technology, Seoul 01811, Republic of Korea; yqma@seoultech.ac.kr (Y.M.); sung-kiuk@seoultech.ac.kr (K.-W.S.)
* Correspondence: hjahn@seoultech.ac.kr; Tel.: +82-2-970-6622
† These authors contributed equally to this work.

Abstract: The oxygen reduction reaction is crucial in the cathode of fuel cells and metal–air batteries. Consequently, designing robust and durable ORR catalysts is vital to developing metal–air batteries and fuel cells. Metal–organic frameworks feature an adjustable structure, a periodic porosity, and a large specific surface area, endowing their derivative materials with a unique structure. In this study, F and N co-doped on the carbon support surface (Co/FN-C) via the pyrolysis of ZIF-67 as a sacrificial template while using Co/FN-C as the non-noble metal catalysts. The Co/FN-C displays excellent long-term durability and electrochemical catalytic performance in acidic solutions. These performance improvements are achieved because the CQDs alleviate the structural collapse during the pyrolysis of ZIF-67, which increases the active sites in the Co nanoparticles. Moreover, F- and N-doping improves the catalytic activity of the carbon support by providing additional electrons and active sites. Furthermore, F anions are redox-stable ligands that exhibit long-term operational stability. Therefore, the well-dispersed Co NPs on the surface of the Co/FN-C are promising as the non-noble metal catalysts for ORR.

Keywords: carbon quantum dots; heteroatom co-doping; oxygen reduction reaction; metal–organic framework; oxygen reduction reaction catalytic activity

Citation: Ma, Y.; Sung, K.-W.; Ahn, H.-J. MOF-Derived Co Nanoparticles Catalyst Assisted by F- and N-Doped Carbon Quantum Dots for Oxygen Reduction. *Nanomaterials* **2023**, *13*, 2093. https://doi.org/10.3390/nano13142093

Academic Editor: Simon Freakley

Received: 23 May 2023
Revised: 10 July 2023
Accepted: 12 July 2023
Published: 18 July 2023

1. Introduction

Owing to the limited reserves and environmental pollution worldwide, concerns regarding fossil fuel depletion have increased. Therefore, highly efficient, renewable, and clean energy sources have received increasing attention [1–3]. Among the various sources of regenerative energy, fuel cells and metal–air batteries are the best prospective chemical energy sources because of their low cost, sizeable energy-converting efficiency, and large theoretical energy density [4,5]. The oxygen reduction reaction (ORR) is one of the two half-reactions indispensable for energy transformation and storage. However, the ORR presents some issues, such as slow electron transfer, low mass transfer efficiency, and slow kinetics, which hinder the practical development of these devices. Therefore, sufficient, stable, and efficient catalysts for the ORR are essential for the efficient operation of the abovementioned devices [6,7]. Among the various catalysts, Pt-based catalysts have attracted widespread attention for their high selectivity and large electrocatalytic activity. High price and low stability hinder their application in energy storage devices [8,9]. Therefore, the non-noble metal catalyst has been extensively explored because of its low cost and excellent stability [10–12]. Despite these advantages, non-noble metal catalysts present critical issues, for example, low catalytic activity, i.e., lower than noble metal-based catalysts. Therefore, the practical design and fabrication of non-noble metal catalysts are crucial to enhancing the catalytic activity of ORRs.

Co-metal catalyst has been extensively studied among non-noble metal catalysts because of their benefits, such as abundant resources, low preparation cost, and bifunctional

catalytic activity [13–17]. However, Co-metal catalysts present some limitations, such as low selectivity and stability, which impede their advanced application [18,19]. Li et al. directly grew Co_3O_4 with Fe-doped nanosheets on Ni foam to overcome these limitations. The synergistic action between Fe and Co atoms enabled an extremely low overpotential and high oxygen-evolving reaction (OER) stability [20]. Huang et al. introduced Mo atoms into a cobalt-based metal–organic framework (MOF) to construct a hierarchical microstructure of CoOx-MoC/N-doped carbon, which showed excellent long-term stability and outstanding OER catalytic activity [21]. Nevertheless, increasing stability and electrocatalytic activity by optimizing the morphology of the catalyst requires further investigation. As self-sacrificing templates, zeolitic imidazolate framework (ZIF), a type of MOF, has been applied to obtain Co-based electrocatalysts with carbon supports via pyrolysis [22]. Furthermore, Co-based electrocatalysts derived from ZIFs exhibit stable catalytic performance in acidic or alkaline electrolytes [23,24]. Especially, Co-NC catalysts involving Co-N_x species manifest significant ORR performances in acidic solutions due to the bonding of nitrogen atoms with cobalt atoms in their porphyrin-like structure. However, due to each atom's high specific surface energy during pyrolysis, Co agglomerates significantly efficiently reduce the utilization of the metal active site [25]. Simultaneously, the polyhedral shape of the ZIFs collapses, which hinders the active site exposure and reduces electrocatalytic activity [26]. Therefore, to maintain the polyhedral structure of the ZIF during pyrolysis, it should be developed as an effective electrocatalyst for ORR. In this regard, well-dispersed electrocatalysts on carbon support that maintains a polyhedral structure and possesses high electrocatalytic activity and stability must be achieved.

Herein, we propose well-dispersed Co nanoparticles (NPs) on an F and N co-doping carbon support (Co/FN-C) by mixing F and N co-doping carbon quantum dots (FNCQDs) with ZIF-67 and performing pyrolysis for non-noble metal catalysts for ORR. Notably, the carbon quantum dots (CQDs) comprise abundant functional groups on their surfaces, which can protect the carbon structure and stabilize the metal NPs during pyrolysis. Therefore, the Co NPs are well distributed on the carbon support surface. Furthermore, the FNCQDs provide F and N atoms into the carbon support. The well-dispersed Co NPs increase electrocatalytic active sites, and F- and N-doping in the carbon support enhances ORR's catalytic stability and activity.

2. Materials and Methods

FNCQDs were fabricated through a hydrothermal process. Specifically, urea (1.24 g, 99.5%, Sigma, St. Louis, MO, USA), sodium fluoride (0.9 g, 99.5%, Sigma), and citric acid (2.73 g, 99%, Sigma) were dissolved entirely in deionized water. The solvent was put into a hydrothermal synthesis autoclave lined with Teflon and heat-treated at 180 °C for 6 h. The obtained solvent was centrifuged thrice (30 min, 10,000 rpm) and then dialyzed for 24 h through a cut-off membrane (molecular weight of 6–8 kD). Finally, to fabricate FNCQDs, the dialysate was dried at 50 °C. The same procedure fabricated N-doped CQDs (NCQDs) without NaF to confirm the effect of F doping. To fabricate an F and N co-doped carbon support (Co/FN-C), 2-methylimidazole (99%, Sigma), cobalt (II) nitrate hexahydrate (98%, Sigma), and FNCQDs were stirred for 6 h in 23 mL of deionized water and obtained after three rounds of centrifugation (5 min, 5000 rpm). The precipitate was dried overnight at 50 °C. In addition, NCQD/ZIF-67 was obtained by replacing the FNCQDs with NCQDs using the same method. Finally, Co/C, Co/N-C, and Co/FN-C were prepared by heating ZIF-67, NCQD/ZIF-67, and FNCQD/ZIF-67 at 750 °C in an Ar atmosphere for 2 h.

The structure, morphology, and elemental distribution of the fabricated sample were investigated via transmission electron microscopy (TEM, Tecnai G2, FEI, Hillsboro, OR, USA), energy dispersive spectroscopy (EDS, Tecnai G2, FEI, Hillsboro, OR, USA) mapping, and field emission scanning electron microscopy (EVO10, Carl Zeiss, FESEM, Oberkochen, Germany), and the surface functional groups, chemical bonding states, and crystal structure of the sample was investigated via Raman spectroscopy (NRS-5100, JASCO, Tokyo, Japan), X-ray photoelectron spectroscopy (XPS, ESCALAB 250, Thermo Fisher, Waltham, MA,

USA), and X-ray diffraction (XRD, Rigaku D/Max-2500 diffractometer, Rigaku, Tokyo, Japan), respectively. Specific surface area and pore structure determined of the sample was investigated by Brunauer–Emmett–Teller (BET, BELSORP-mini II, BEL Japan INC, Osaka, Japan).

Potentiostat/galvanostat (Ecochemie Autolab, PGST302N, Metrohm, Utrecht, The Netherlands) for measuring the electrochemical performance of catalysts. This potentiostat/galvanostat has a rotating disc electrode and an electrochemical workstation with a speed controller. The three-electrode assembly comprised a working electrode, a reference electrode, and a counter electrode. Homogeneous inks, which contained 10 mg of the fabricated samples as a catalyst in Nafion® perfluorinated resin solution (57.2 μL), deionized water (50 μL), and 2-propanol (900 μL), were prepared via dispersion through sonication 30 min and string 12 h. The ink (1.8 μL) was dispersed on the working electrode surface (area: 0.0706 cm^2) and dried (30 min, 50 °C) before the measurement was performed. Cyclic voltammetry (CV) was performed in Ar and O_2 saturated 0.1 M $HClO_4$ electrolyte. Linear sweep voltammetry (LSV) was measured at rotational speeds of 100, 400, 900, and 1600 and a scanning rate of 5 mV/s in O_2-saturated 0.1 M $HClO_4$ electrolyte. Finally, the accelerated durability test (ADT) was tested at a scanning rate of 100 mV/s for 5000 cycles to confirm the long-term electrocatalytic stability. LSV results were re-tested again at 1600 rpm after the ADT.

3. Result and Discussion

Figure 1 illustrates a diagram graphic of the fabricating method for the (a) FNCQDs, (b) FNCQD/ZIF-67, and (c) Co/FN-C. The FNCQDs were fabricated through a hydrothermal process. Urea provided the N source, sodium fluoride provided the F source, and citric acid provided the C source. FNCQD/ZIF-67 was fabricated by stirring FNCQDs and ZIF-67. Finally, F- and N-doped carbon-supported cobalt NPs were obtained via the pyrolysis of FNCQD/ZIF-67. During the pyrolysis, carbon support was formed from ZIF-67 as a sacrificial template, and Co NPs were forming on the surface of carbon support owing to the diffusion of Co atoms in ZIF-67. The CQDs effectively maintained the structure of the sacrificial template of ZIF-67; therefore, the Co NPs were well dispersed on the carbon support surface, thus increasing electrocatalytic active sites. Furthermore, F and N were doped into the carbon support via F and N atoms from the FNCQDs during pyrolysis, which enhanced the catalytic stability and ORR activity of the Co/FN-C.

Figures S1 and S2 show the TEM and EDS mapping of NCQD and FNCQD. The NCQD and FNCQD particles were uniform in size with a diameter of ~5.0 nm (Figures S1a and S2a) and the lattice fringe space is about 0.32 nm, representing the (002) plane of graphite (Figures S1b and S2b). In Figure S1c, the EDS mapping indicated that C and N atoms were present in the NCQDs. Meanwhile, as shown in Figure S2c, the EDS results indicated that C, F, and N existed in the FNCQDs. This indicates that we have successfully prepared F- and N-doped CQDS.

To confirm the elemental distribution, the TEM-EDS mapping of the (a) ZIF-67, (b) NCQD/ZIF-67, and (c) FNCQD/ZIF-67 was performed (Figure S3). The TEM images of the three samples exhibited a polygonal structure with a size ranging from ~365 to ~395 nm. The EDS mapping indicated that C, Co, and N existed in the ZIF-67, NCQD/ZIF-67, and FNCQD/ZIF-67. Furthermore, only FNCQD/ZIF-67 showed F atoms. This shows that F atoms can be doped at Co/FN-C after pyrolysis of FNCQD/ZIF-67.

As shown in Figure S4, the XRD pattern was analyzed to check the crystal structures of ZIF-67, NCQD/ZIF-67, and FNCQD/ZIF-67. All samples exhibited sharp diffraction peaks at 7.4°, 10.4°, 12.6°, 14.7°, 16.5°, 18.1°, 22.2°, 24.5°, 25.6°, 26.7°, 29.6°, 31.5°, and 32.4° which was attributed to the (011), (002), (112), (022), (013), (222), (114), (233), (002), (134), (044), (244), and (235) planes of simulate ZIF-67 [27]. The intensity of the diffraction peak at 12.6° for NCQD/ZIF-67 and FNCQD/ZIF-67 nanocomposites is lower than that of pure ZIF-67, suggesting that the crystal structure of ZIF-67 changes with the formation of the composites. Figure S5 shows the N_2 adsorption–desorption isotherms of ZIF-67,

NCQD/ZIF-67, and FNCQD/ZIF-67. Three samples all displayed type-I isotherms. The BET surface areas of ZIF-67, NCQD/ZIF-67, and FNCQD/ZIF-67 were 1152.2, 1166.6, and 1158.5 m^2 g^{-1}, respectively (Figure S5a). The results showed that the surface areas of ZIF-67, NCQD/ZIF-67, and FNCQD/ZIF-67 were almost the same and had a higher specific surface area [28].

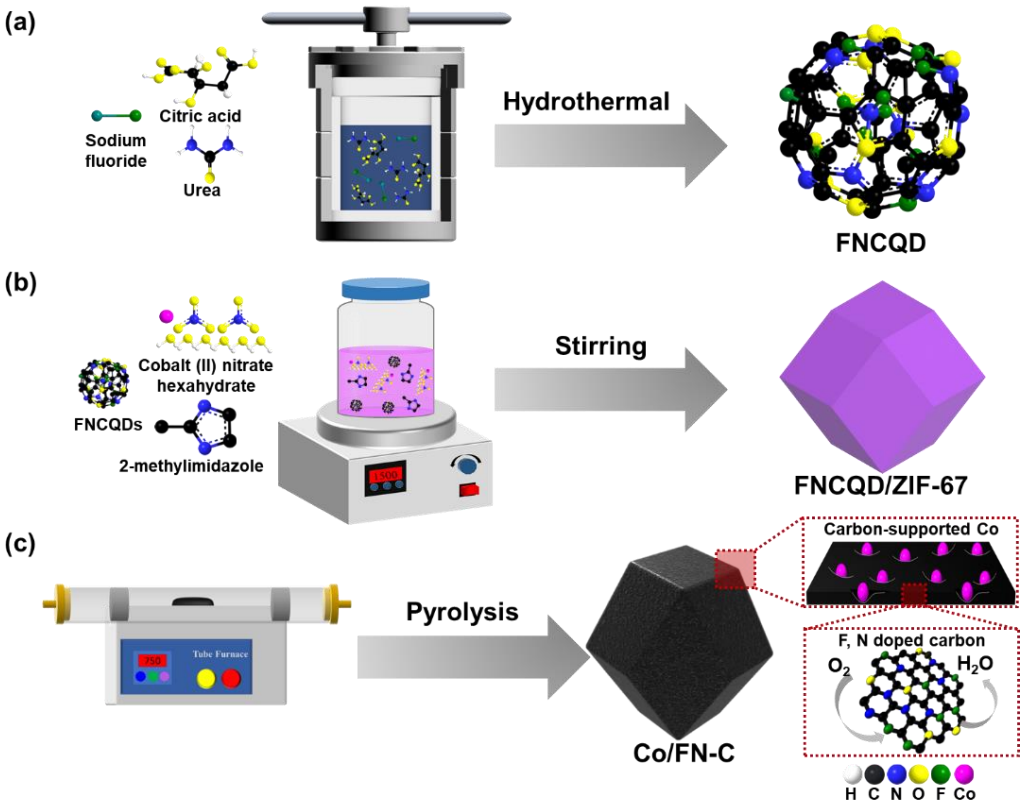

Figure 1. Schematic image of fabricating process about (**a**) FNCQDs, (**b**) FNCQD/ZIF-67, and (**c**) Co/FN-C.

FESEM was conducted on all samples to examine their morphology (see Figure 2). Figure 3a shows that Co/C sizes of ~295 to ~353 nm exhibited a collapsed polyhedral structure. During the pyrolysis of ZIF-67, shrinkage occurred because of the dehydration of the organic components under anaerobic conditions [29,30]. Furthermore, the Co NPs agglomerated because of the significant surface energy of the single atoms, significantly reducing the active sites' efficiency utilization [31]. However, Co/N-C and Co/FN-C (Figure 2a,b, respectively), exhibited polyhedral structures and bumpy surfaces with sizes of ~350 to ~410 nm. The unchanged polyhedral structure of Co/FN-C and Co/N-C was due to the CQDs, which served as protective layers. The plentiful oxidized functional groups of the CQDs strongly coordinate with the Co nodes in ZIF-67. Subsequently, ZIF-67 is pyrolyzed, and the CQDs interact strongly with ZIF-67 alleviating the structure collapse while preventing the severe aggregation of adjacent Co, thus affording well-dispersed Co NPs on the carbon support surface [32–34]. This confirmed that carbon support derived from ZIF-67 as a sacrificial template was fabricated successfully and enabled a polyhedral structure to be maintained via the CQDs.

To characterize the nanostructures, a TEM analysis of the Co/FN-C was performed. As shown in Figure 3a, relatively dark spots of Co NPs in the size range of ~15 to ~52 nm were observed with the relatively bright region of the carbon support, which exhibited a polygonal structure with sizes from ~378 to ~398 nm. Furthermore, Figure 3b shows that the bright region featuring the lattice fringe space is about 0.34 nm, representing the (002) plane of graphite, whereas the dark spot featuring the lattice fringe space is about 0.17 nm, representing the (200) plane of Co. To confirm the elemental distribution, a TEM-EDS

mapping of the Co/FN-C was performed (Figure 3c). The EDS results indicated that C, N, F, and Co were uniform dispersion along the NPs and carbon support. These results prove that the Co NPs were well dispersed in the Co/FN-C, thus enhancing the electrocatalytic activity by increasing the active sites in the Co NPs.

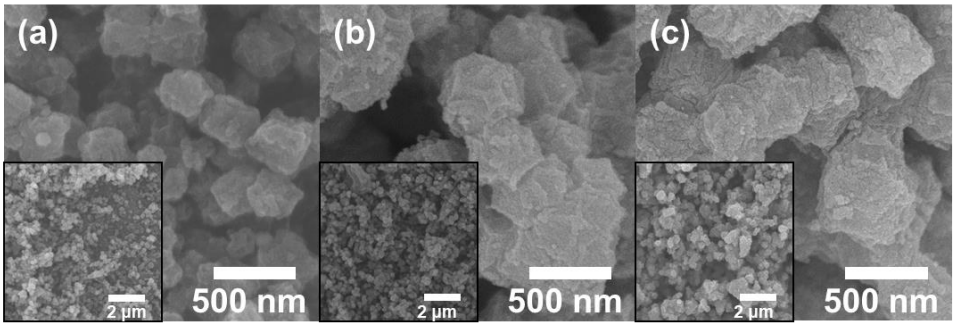

Figure 2. FESEM images for the as-prepared (**a**) Co/C, (**b**) Co/N-C, and (**c**) Co/FN-C.

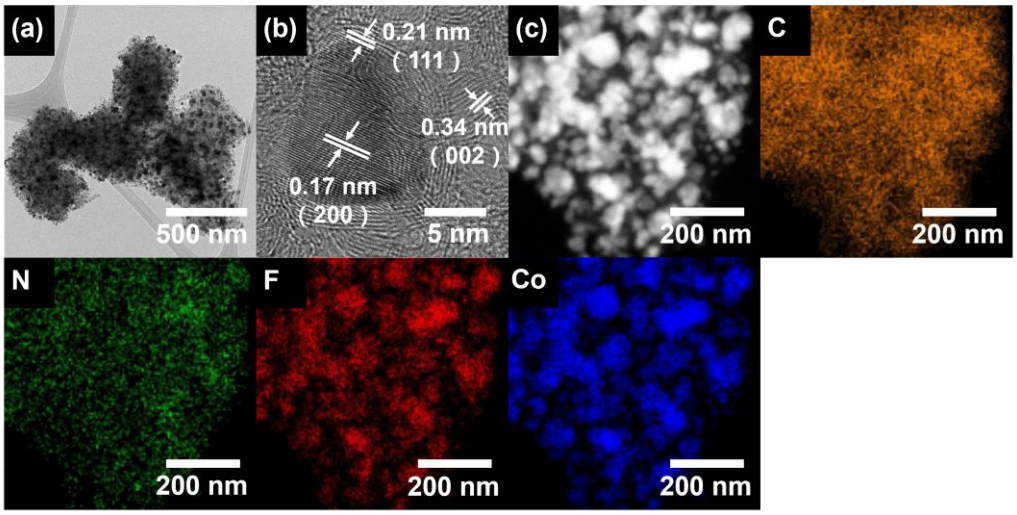

Figure 3. (**a**) Low- and (**b**) high-resolution TEM images, and (**c**) EDS mapping of C, N, F, and Co of Co/FN-C.

Figure 4a shows that the XRD pattern was analyzed to investigate the crystal structures of three samples. All samples showed a broad peak of diffraction at ~24.6°, which corresponds to the (002) plane of graphite (JCPDS 65-6212), and sharp peaks of diffraction at ~75.9°, ~51.3°, and ~44.2°, which corresponds to the (220), (200), and (111) planes of Co (JCPDS 15-0806) [35,36]. Peaks other than those of amorphous graphite and metallic Co were not observed, indicating that all the Co^{2+} in ZIF-67 was completely reduced to metallic Co during pyrolysis. The graphitization degrees of three samples were determined using Raman spectroscopy (Figure 4b). Three samples exhibited two characteristic Raman absorption peaks within the compass of 1000–1800 cm^{-1} (1350 cm^{-1}: D-band absorption peak, 1580 cm^{-1}: G-band absorption peak). Theoretically, the G bands belong to the order of the degree of the sp^2 carbon graphitic structures, and the D bands represent the disorder and defects of the sp^3 hybridized carbon. The material's graphitizing degree is compared through I_D/I_G [37,38]. Compared with Co/C (1.010), Co/FN-C and Co/N-C exhibited significantly large I_D/I_G of 1.032 and 1.028, suggesting that the F and N atoms doping induced defects in the carbon lattice and exposed the edge plane. ORR activity was generated by activating the π electrons, which was achieved by disrupting the integrity of its π-conjugated structure. Therefore, F and N doping in sp^2 carbons resulted in defects by breaking the integrity of its π-conjugated structure, thus enhancing the activity of the ORR [39–42].

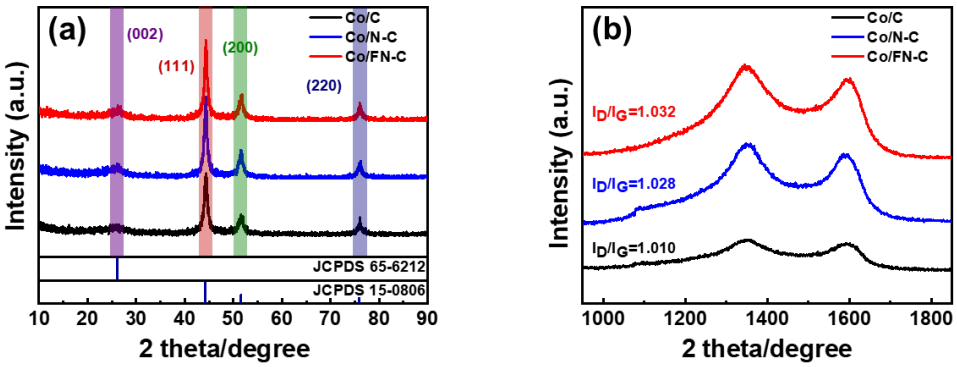

Figure 4. (**a**) X-ray patterns and (**b**) RAMAN spectrum of Co/C, Co/N-C, and Co/FN-C.

Figure 5 shows that the chemical bonding states of Co/C, Co/N-C, and Co/FN-C were analyzed using XPS. The C 1s XPS profiles of all samples exhibited three characteristic peaks, which corresponded to O=C-O/C-F groups (~288.95 eV), C-N groups (~286.47 eV), and C-C groups (~284.71 eV). Co/FN-C and Co/N-C showed larger C-N peaks compared to Co/C because of the additional N doping owing to the FNC-QDs [43]. The N 1s XPS profiles showed the peaks of graphitic N (~400.80 eV), pyrrolic N (~399.99 eV), Co-N (~399.09 eV), and pyridinic N (~397.35 eV) (Figure 5b). Via the aromatic system, pyridinic N supplies two p-electrons, whereas pyrrolic-N provides one p-electron, thus resulting in increased catalytic activity [44,45]. Two core-level signal peaks at ~781.84 eV and ~797.50 eV were visible in the XPS spectrum of Co 2p (Figure 5d), corresponded to Co $2p_{3/2}$ and Co $2p_{1/2}$, and minor peaks of the Co^{2+} satellite (~802.67, ~786.86 eV), and Co-N (~779.31 eV). Furthermore, only Co/FN-C showed two peaks at ~684.6 and ~687.6eV in the F 1s XPS spectra, which represent the semi-ionic and covalent bonds of C-F, owing to the F atoms in the FNCQDs (Figure 5c). The doped F atoms can enhance the number of edge defects of the carbon lattice, thus providing more electrocatalytic active sites [46]. Furthermore, F anions provide redox-stable ligands, which can effectively improve catalytic stability [47,48].

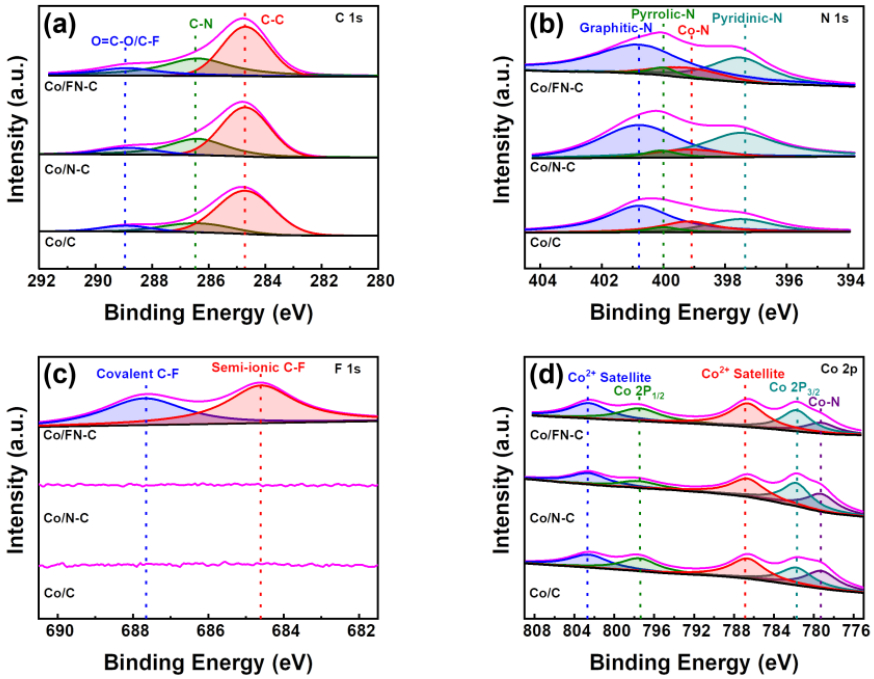

Figure 5. XPS spectrum (**a**) C 1s, (**b**) N 1s, (**c**) F 1s, and (**d**) Co 2p of Co/C, Co/N-C, and Co/FN-C.

Figure 6a–c shows the electrochemical activities of the Co/C, Co/N-C, and Co/FN-C electrodes measured via CV with different scanning rates from 10 to 100 m V s^{-1}. All electrodes showed quasi-rectangular CV curves, which is characteristic of the charge and discharge process of electrostatic double-layer capacitors [49]. Moreover, we evaluated the electrochemical active surface area (ECSA), which is an indicator for comparing active sites of catalysts involved in the electrochemical reaction and is generally considered an important parameter for high ORR performance. In a without Faradaic potential window (0.1–0.3 V) [50–55], the C_{dl} (electrical double layer capacitance) and ECSA were tested and calculated by CV at different scanning rates as follows [56,57]:

$$C_{dl} = j/r \quad (1)$$

$$ECSA = C_{dl} / C_{s,} \quad (2)$$

where r corresponds to the scan rate, C_s corresponds to the specific capacitance (C_s = 0.035 mF/cm^2), and j corresponds to the current density. Figure 6d shows that the C_{dl} values of the Co/C, Co/N-C, and Co/FN-C electrodes were 30.9, 45.4, and 62.9 mF cm^{-2}, respectively [45]. Meanwhile, their ECSA values were 882.8, 1297.1, and 1797.1 cm ^{2}, respectively (Figure 6e). The largest ECSA shown by the Co/FN-C electrode indicates that improved electrocatalytic active sites by the well-dispersed Co NPs on the carbon support increased the defects by N- and F-doping in carbon and effectively extended the electrochemically available active sites, unlike the cases with the other electrodes [58].

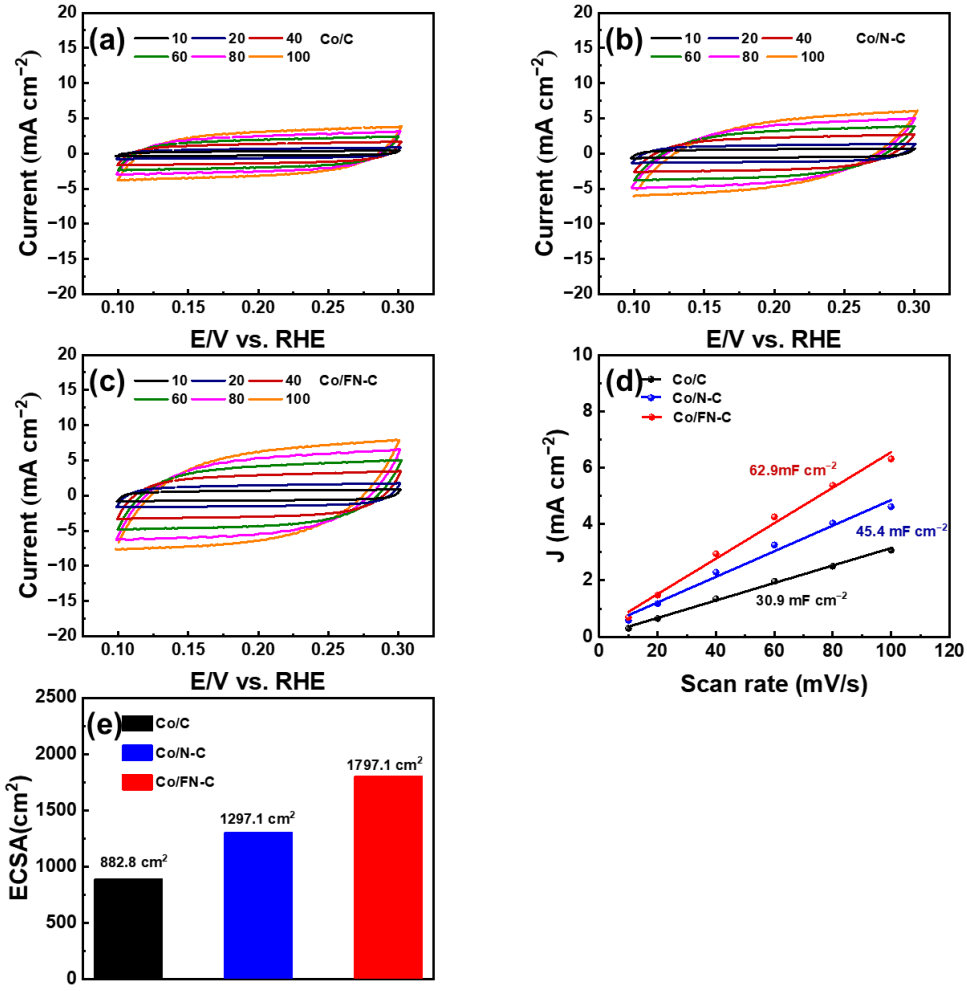

Figure 6. Cyclic voltammetry curve of (**a**) Co/C, (**b**) Co/N-C, (**c**) Co/FN-C (**d**) C_{dl} linear fitting (**e**) ECSA values for Co/C, Co/N-C, and Co/FN-C.

As shown in Figure 7a, to understand the electrochemical activity more comprehensively, LSV measurement was employed. The Co/FN-C electrode showed excellent ORR activities, including a limited current density of $-4.678\ mA/cm^2$, a half-wave potential ($E_{1/2}$) of 0.702 V, and an onset potential (E_{onset}) of 0.917 V, compared with the Co/C and Co/N-C electrodes (Co/C: a limited current density of $-2.923\ mA/cm^2$, $E_{1/2}$: 0.702 V, E_{onset}: 0.840 V; NCQD/Co/C: a limited current density of $-4.678\ mA/cm^2$, $E_{1/2}$: 0.745 V, E_{onset}: 0.888 V). Compared with other published papers, Co/FN-C sample outperformed the E_{onset} and $E_{1/2}$ (Table 1) [50,59–62]. Furthermore, there are two main electronic pathways for the reduction of O_2. In the direct 4-electron reaction, the single oxygen bond directly cleavage to generate H_2O with high reaction efficiency, whereas the 2-electron reduction of the H_2O_2 intermediate is not only a low-efficiency ORR but also increases the ORR overpotential and corrodes the carbon catalyst support. Therefore, the reduction of H_2O_2 through the 4-electron pathway is conducive to the ORR [63]. The amount of oxygen reduction electron (n) was calculated through the Koutecky–Levich Formula (K–L) (3) and (4) [37].

$$\frac{1}{j} = \frac{1}{j_d} + \frac{1}{j_k} = \frac{1}{B\omega^{\frac{1}{2}}} + \frac{1}{j_k} \tag{3}$$

$$B = 0.62^{n} F C_0 (D_0)^{\frac{2}{3}} V^{-\frac{1}{6}} \tag{4}$$

where j is the measured current, j_d corresponds to the limiting current, j_k corresponds to the kinetic current, measured current, and limiting current, B corresponds to the proportionality coefficient, which is calculated using Equation (4); ω corresponds to the rate of angular rotation of the electrode ($\omega = 2\ n^*\pi/60$, where n* corresponds to the number of rotations of the electrode per minute); n corresponds to the electrons transferred number when reducing one oxygen; C_0 corresponds to the solubility of oxygen in the solution; v corresponds to the kinetic viscosity coefficient; Faraday constant is 96,485 C/mol; and D_0 corresponds to the diffusion coefficient. To identify the ORR performance more clearly, the LSV result of the Co/FN-C electrode was measured at 100–1600 rpm (Figure 8a). According to the above formula, the electron transfer number in the 0.2–0.4 V (vs. RHE) range was 3.98 (about 4) (Figure 8b). Therefore, the Co/FN-C electrode induced an excellent ORR process in an acidic electrolyte owing to the 4-electron pathway, which was ascribed to the increased electrochemically active sites by the uniform dispersed of Co NPs on the carbon support and increased ORR activity by F and N doping in carbon [64,65]. Furthermore, to confirm the electrocatalytic stability, we compared the LSV curves of the three electrodes before and after CV for 5000 cycles (Figure 7b–d). After 5000 cycles, the Co/FN-C electrode showed the lowest potential degradation at $\Delta E_{1/2}$ = 2.1 mV compared with the Co/C (41.7 mV) and Co/N-C (5.4 mV) electrodes. The catalytic stability of the Co/FN-C electrode is excellent because F anions, as redox-stable ligands, are electron-withdrawing groups that effectively reduce the electron cloud density of carbon materials, thereby increasing their resistance to oxidative degradation. Furthermore, F anions can reduce the electron densities of metal nuclei ions and then increase the polarity of metal compounds, thereby improving the catalytic stability of the ORR. The following factors are responsible for this excellent electrochemical performance and stability: (1) the well-dispersed Co NPs, which increased the catalytic active sites; (2) F and N doping in carbon, which enhanced the catalytic activity; and (3) the redox-stable ligand by F anions, which reinforced the catalytic stability. To test the stability of the electrode in 0.1 M $HClO_4$, we added Co/C, Co/N-C, and Co/FN-C to 0.1 M $HClO_4$ overnight and examined their crystal structure by XRD. Figure S6 shows the XRD patterns of before and after $HClO_4$ treatment of Co/C, Co/N-C, and Co/FN-C samples. All samples showed a broad peak of diffraction at ~24.6°, which corresponds to the (002) plane of graphite (JCPDS 65-6212), and sharp peaks of diffraction at ~75.9°, ~51.3°, and ~44.2°, which corresponds to the (220), (200), and (111) planes of Co (JCPDS 15-0806), which means that the crystal structure of all samples was maintained after $HClO_4$ treatment. Meanwhile, we add SEM-EDS mapping images and chemical composition before and after the electrochemical test of the Co/FN-C electrode, as shown in Figure S7 and Table S1.

After the $HClO_4$ treatment, the elements were well dispersed, and the atomic percentage of Co is maintained. Therefore, these results also indicate that the Co/FN-C sample can be electrochemically tested in $HClO_4$.

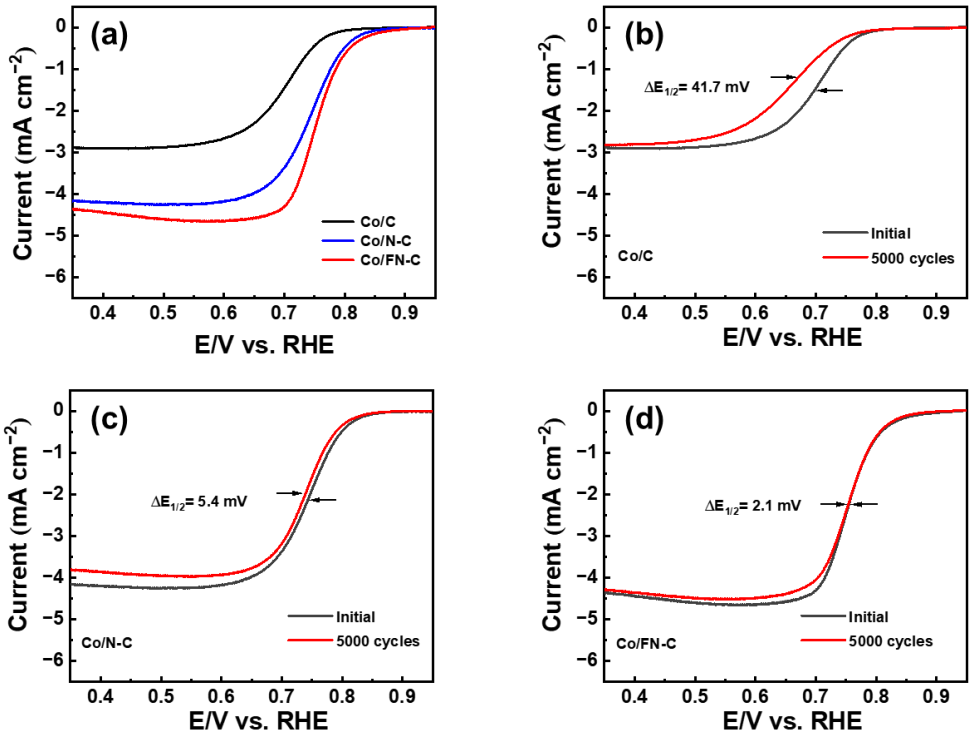

Figure 7. (**a**) Linear sweep voltammetry curves initial and ADT of (**b**) Co/C, (**c**) Co/N-C, and (**d**) Co/FN-C.

Table 1. Compared to other published papers the value of E_{onset} and $E_{1/2}$.

Material	E_{onset} (V)	$E_{1/2}$ (V)
Co-NSC 200	0.81	0.74
Fe-N-C	0.85	0.74
CAPANI-Fe-NaC	Not mentioned	0.73
PNGr	0.87	0.64
FeCo/C680	0.9	0.76
Co/FN-C	0.917	0.753

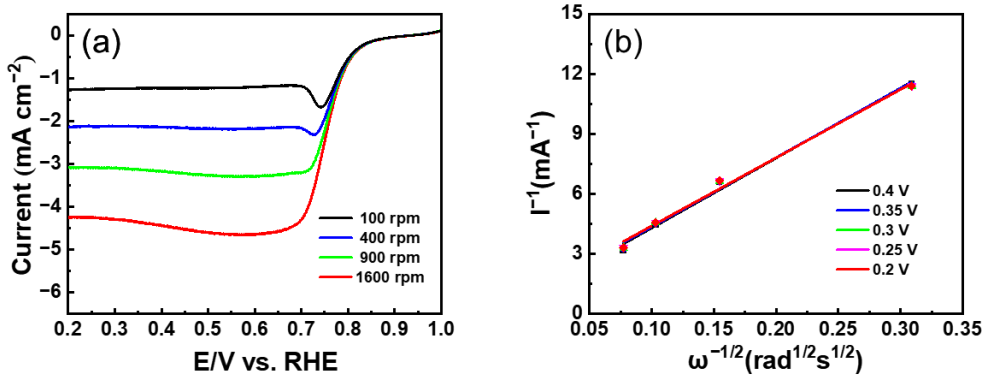

Figure 8. (**a**) LSV curves at various rotating speeds (**b**) Koutecky–Levich plots at different voltages of Co/FN-C.

4. Conclusions

In this study, we fabricated well-dispersed Co NPs on F and N carbon supports using ZIF-67 as a sacrificial template for an ORR catalyst. During the pyrolysis of ZIF-67 to obtain Co NPs with carbon support, the mixed FNCQDs alleviated the structural collapse of ZIF-67 and doped the carbon support with F and N atoms. The Co/FN-C electrode showed excellent ORR activities, including an ECSA of 3028.0 cm^{-2}, a limited current density of -4.678 mA/cm^2, $E_{1/2}$ of 0.702 V, and an E_{onset} of 0.917 V. Simultaneously, the Co/FN-C electrode induced an excellent ORR in an acidic electrolyte because of the 4-electron pathway. Furthermore, after 5000 cycles, the Co/FN-C exhibited excellent long-term stability with an $\Delta E_{1/2}$ of only 2.1 mV. These performance improvements are attributed to: First, the well-dispersed Co NPs increase the active sites, thus alleviating the structural collapse of the CQDs during pyrolysis and improving the active sites number. Second, the F and N co-doping in the carbon support enhanced catalytic activity, which provided additional electrons and increased the number of edge defects. Finally, F anions, which served as redox-stable ligands, reinforced the catalytic stability. In conclusion, dispersing Co NPs uniformly in Co/FN-C is a prospective strategy for non-precious metal catalysts to be used in the ORR.

Supplementary Materials: The following supporting information can be downloaded at: https://www.mdpi.com/article/10.3390/nano13142093/s1, Figure S1: (a) Low- and (b) high-resolution TEM images, (c), EDS mapping results of NCQD; Figure S2: (a) Low- and (b) high-resolution TEM images, (c), EDS mapping results of FNCQD; Figure S3: TEM-EDS mapping results of (a) ZIF-67, (b) NCQD/ZIF-67, and (c) FNCQD/ZIF-67; Figure S4: XRD patterns of ZIF-67, NCQD/ZIF-67 and FNCQD/ZIF-67; Figure S5: (a) BET gas adsorption plots, (b) change on BET of ZIF-67, NCQD/ZIF-67 and FNCQD/ZIF-67; Figure S6: X-ray patterns of (a) before and (b) after $HClO_4$ treatment of Co/C, Co/N-C, and Co/FN-C; Figure S7: SEM-EDS mapping of C, N, F, and Co of (a) before and (b) after electrochemical test of Co/FN-C electrode; Table S1: The chemical composition (atomic percent) of before and after the electrochemical test of Co/FN-C electrode.

Author Contributions: Y.M. and K.-W.S. made equally important contributions to this research. The investigation, Y.M.; methodology and writing, Y.M. and K.-W.S.; writing—comment, K.-W.S.; writing—comment, editing, and supervision conceptualization and review and editing, H.-J.A. All authors have read and agreed to the published version of the manuscript.

Funding: This work was sponsored by the Nano and Material Technology Development Program through the National Research Foundation of Korea (NRF) funded by the Ministry of Science and ICT (2021M3H4A3A02086102) and the Basic Science Research Program through the National Research Foundation of Korea (NRF) funded by the Ministry of Education (NRF-2021R1A6A1A03039981).

Data Availability Statement: All data generated or analyzed during this work are included in this published article.

Conflicts of Interest: The authors declare no conflict of interest.

References

1. Lu, J.; Li, L.; Park, J.B. Aprotic and aqueous Li–O_2 batteries. *Chem. Rev.* **2014**, *114*, 5611–5640. [CrossRef] [PubMed]
2. Bilgen, S. Structure and environmental impact of global energy consumption. *Renew. Sustain. Energ. Rev.* **2014**, *38*, 892–902. [CrossRef]
3. Ibrahim, D. Renewable energy and sustainable development: A crucial review. *Renew. Sustain. Energ. Rev.* **2000**, *4*, 157–175.
4. Peng, B.; Chen, J. Functional materials with high-efficiency energy storage and conversion for batteries and fuel cells. *Coord. Chem. Rev.* **2009**, *253*, 2805–2813. [CrossRef]
5. Lee, J.S.; Kim, S.T.; Cao, R.; Choi, N.S. Metal-air batteries with high energy density: Li–air versus Zn–air. *Adv. Energy Mater.* **2010**, *1*, 34–50. [CrossRef]
6. Shi, Z.; Yang, W.; Gu, Y.; Sun, Z. Metal-nitrogen-doped carbon materials as highly efficient catalysts: Progress and rational design. *Adv. Sci.* **2020**, *7*, 2001069. [CrossRef]
7. Bezerra, L.S.; Maia, G. Developing efficient catalysts for the OER and ORR using a combination of Co, Ni, and Pt oxides along with graphene nanoribbons and $NiCo_2O_4$. *J. Mater. Chem. A* **2020**, *8*, 17691–17705. [CrossRef]
8. Liu, M.; Zhao, Z.; Duan, X.; Huang, Y. Nanoscale Structure Design for High-Performance Pt-Based ORR Catalysts. *Adv. Mater.* **2018**, *31*, 1802234. [CrossRef]

9. He, C.; Ma, Z.; Wu, Q. Promoting the ORR catalysis of Pt-Fe intermetallic catalysts by increasing atomic utilization and electronic regulation. *Electrochim. Acta* **2020**, *330*, 135119. [CrossRef]
10. Wei, B.; Fu, Z.H.; Legut, D.; Germann, T.C.; Du, S.; Zhang, H.; Francisco, J.S.; Zhang, R.F. Rational design of highly stable and active MXene-based bifunctional ORR/OER double-atom catalysts. *Adv. Mater.* **2021**, *33*, 2102595. [CrossRef]
11. Dou, S.; Wang, X.; Wang, S. Rational design of transition metal—Based materials for highly efficient electrocatalysis. *Small Methods* **2019**, *3*, 1800211. [CrossRef]
12. Zhang, L.; Wilkinson, D.P.; Liu, Y.; Zhang, J.J. Progress in nanostructured (Fe or Co)/N/C non-noble metal electrocatalysts for fuel cell oxygen reduction reaction. *Electrochim. Acta* **2018**, *262*, 326–336. [CrossRef]
13. Jin, H.; Yu, R.; Hu, C.; Ji, P.; Ma, Q.; Liu, B.; He, D.; Mu, S. Size-controlled engineering of cobalt metal catalysts through a coordination effect for oxygen electrocatalysis. *Appl. Catal. B Environ.* **2022**, *317*, 121766. [CrossRef]
14. Jiang, S.; Zhu, C.; Dong, S. Cobalt and nitrogen—Cofunctionalized graphene as a durable non-precious metal catalyst with enhanced ORR activity. *J. Mater. Chem. A* **2013**, *1*, 3593–3599. [CrossRef]
15. Wang, P.; Zhang, L.; Wang, Z.; Bu, D.; Zhan, K.; Yan, Y.; Yang, J.; Zhao, B. N and Mn dual-doped cactus-like cobalt oxide nanoarchitecture derived from cobalt carbonate hydroxide as efficient electrocatalysts for oxygen evolution reactions. *J. Colloid Interface Sci.* **2021**, *597*, 361–369. [CrossRef] [PubMed]
16. David, S.C.; Nora, H.L. Single-atom catalysis for carbon dioxide dissociation using greigite-supported $M_1/Fe_3S_4(111)$ (M = Sc, Ti, V, Cr, Mn, Fe, Co, Ni, Cu, Zn) under electrostatic fields. *J. Catal. Sci.* **2023**, *425*, 89–104.
17. Li, Y.; Li, W.; Fang, M. The preparation, performance and lithiation mechanism of cobalt-doped zinc oxide as a high performance anode material for LIB. *Curr. Appl. Phys.* **2017**, *17*, 1050–1057. [CrossRef]
18. Yuan, N.; Jiang, Q.; Li, J.; Tang, J. A review on non-noble metal based electrocatalysis for the oxygen evolution reaction. *Arab. J. Chem.* **2020**, *13*, 4294–4309. [CrossRef]
19. Li, X.; Liu, G.; Popov, B. Activity and stability of non–precious metal catalysts for oxygen reduction in acid and alkaline electrolytes. *J. Power Sources Adv.* **2010**, *195*, 6373–6378. [CrossRef]
20. Li, Y.; Li, F.; Meng, X.; Wu, X.; Li, S.; Chen, Y. Direct chemical synthesis of ultrathin holey iron doped cobalt oxide nanosheets on nickel foam for oxygen evolution reaction. *Nano Energy* **2018**, *54*, 238–250. [CrossRef]
21. Huang, T.; Chen, Y.; Lee, J.M. A microribbon hybrid structure of CoO_x–MoC encapsulated in N–doped carbon nanowire derived from MOF as efficient oxygen evolution electrocatalysts. *Small* **2017**, *13*, 1702753. [CrossRef] [PubMed]
22. Huang, C.; Ji, Q.; Zhang, H. Ru-incorporated Co_3O_4 nanoparticles from self-sacrificial ZIF-67 template as efficient bifunctional electrocatalysts for rechargeable metal-air battery. *J. Colloid Interface Sci.* **2022**, *606*, 654–665. [CrossRef] [PubMed]
23. He, Y.; Wang, Z.; Wang, H. Metal-organic framework-derived nanomaterials in environment related fields: Fundamentals, properties and applications. *Coord. Chem. Rev.* **2021**, *429*, 213618. [CrossRef]
24. Ren, Y.; Wang, X.; Ma, J.; Zheng, Q. Metal-organic framework-derived carbon–based composites for electromagnetic wave absorption: Dimension design and morphology regulation. *J. Mater. Sci. Technol.* **2023**, *132*, 223–251. [CrossRef]
25. Song, K.; Feng, Y.; Zhang, W.; Zheng, W. MOFs fertilized transition–metallic single–atom electrocatalysts for highly-efficient oxygen reduction: Spreading the synthesis strategies and advanced identification. *J. Energy Chem.* **2022**, *67*, 391–422. [CrossRef]
26. Wang, G.; Deng, J.; Yan, T.; Zhang, J.; Shi, L.; Zhang, D. Turning on electrocatalytic oxygen reduction by creating robust Fe-N_x species in hollow carbon frameworks via in situ growth of Fe doped ZIFs on g-C_3N_4. *Nanoscale* **2020**, *12*, 5601–5611. [CrossRef]
27. Mahboobeh, S.; Mojtaba, M. Synthesis and characterization of GO/ZIF-67 nanocomposite: Investigation of catalytic activity for the determination of epinine in the presence of dobutamine. *Micromachines* **2022**, *13*, 88.
28. Panchariya, D.; Rai, R.; Kumar, E.; Singh, S. Core–shell zeolitic imidazolate frameworks for enhanced hydrogen storage. *ACS Omega* **2018**, *3*, 167–175. [CrossRef] [PubMed]
29. Qin, J.N.; Wang, S.B.; Wang, X.C. Visible-light reduction CO_2 with dodecahedral zeolitic imidazolate framework ZIF-67 as an efficient co-catalyst. *Appl. Catal. B Environ.* **2017**, *209*, 476–482. [CrossRef]
30. Gong, H.M.; Zhang, X.J.; Wang, G.R.; Liu, Y.; Li, Y.B.; Jin, Z.L. Dodecahedron ZIF-67 anchoring ZnCdS particles for photocatalytic hydrogen evolution. *Mol. Catal.* **2020**, *485*, 110832. [CrossRef]
31. Zhang, H.; Liu, G.; Shi, L.; Ye, J. Single-Atom Catalysts: Emerging Multifunctional Materials in Heterogeneous Catalysis. *Adv. Energy Mater.* **2018**, *8*, 1701343. [CrossRef]
32. Wu, H.; Wu, M.; Wang, B.; Yong, X.; Liu, Y.; Li, B.; Liu, B.; Lu, S. Interface electron collaborative migration of Co–Co_3O_4/carbon dots: Boosting the hydrolytic dehydrogenation of ammonia borane. *J. Energy Chem.* **2020**, *48*, 43–53. [CrossRef]
33. Meng, X.; Zhang, C.; Dong, C.; Sun, W.; Ji, D.; Ding, Y. Carbon quantum dots assisted strategy to synthesize Co@ Nc for boosting photocatalytic hydrogen evolution performance of Cds. *Chem. Eng. J.* **2020**, *389*, 124432. [CrossRef]
34. Wu, C.; Chen, X.; Tang, L.; Wei, Q.; Wei, X.; Liang, J.; Wang, L. Rationally constructing a nano MOF-derived Ni and CQD embedded N-doped carbon nanosphere for the hydrogenation of petroleum resin at low temperature. *ACS Appl. Mater. Interfaces* **2021**, *13*, 10855–10869. [CrossRef]
35. Zhao, C.; Jiao, Y.; Hu, F. Green synthesis of carbon dots from pork and application as nanosensors for uric acid detection, Spectrochim. *Acta Part A Mol. Biomol. Spectrosc.* **2018**, *190*, 360–367. [CrossRef]
36. Wang, L.; Wang, Z.H.; Xie, L.L.; Zhu, L.M.; Cao, X.Y. ZIF-67-derived N-doped Co/C nanocubes as high–performance anode materials for lithium-ion batteries. *ACS Appl. Mater. Interfaces* **2019**, *11*, 16619–16628. [CrossRef] [PubMed]

37. Ferrari, A.C.; Basko, D.M. Raman Spectroscopy as a Versatile Tool for Studying the Properties of Graphene. *Nat. Nanotechnol.* **2013**, *8*, 235–246. [CrossRef] [PubMed]
38. Ćirić-Marjanović, G.; Pašti, I.; Gavrilov, N.; Janošević, A.; Mentus, S. Carbonised polyaniline and polypyrrole: Towards advanced nitrogen-containing carbon materials. *Chem. Pap.* **2013**, *67*, 781–813. [CrossRef]
39. Yang, L.J.; Jiang, S.J.; Zhao, Y.; Zhu, L.; Chen, S.; Wang, X.Z.; Wu, Q.; Ma, J.; Ma, Y.W.; Hu, Z. Boron-doped carbon nanotubes as metal–free electrocatalysts for the oxygen reduction reaction. *Angew. Chem. Int. Ed.* **2011**, *50*, 7132–7135. [CrossRef]
40. Wu, Q.; Yang, L.; Wang, X.; Hu, Z. Mesostructured carbon—Based nanocages: An advanced platform for energy chemistry. *Adv. Mater.* **2020**, *32*, 1904177. [CrossRef]
41. Zhao, Y.; Yang, L.; Chen, S.; Wang, X.; Ma, Y.; Wu, Q.; Jiang, Y.; Qian, W.; Hu, Z. Can boron and nitrogen co-doping improve oxygen reduction reaction activity of carbon nanotubes? *J. Am. Chem. Soc.* **2013**, *135*, 1201–1204. [CrossRef]
42. Behan, J.A.; Mates-Torres, E.; Stamatin, S.N.; Dominguez, C.; Iannaci, A.; Fleischer, K.; Hoque, M.K.; Perova, T.S.; Garcia-Melchor, M.; Colavita, P.E. Untangling cooperative effects of pyridinic and graphitic nitrogen sites at metal–free N doped carbon electrocatalysts for the oxygen reduction reaction. *Small* **2019**, *15*, 1902081. [CrossRef]
43. Wu, X.; Zhao, B.; Zhang, J.; Xu, H.; Xu, K.; Chen, G. Photoluminescence and photodetecting properties of the hydrothermally synthesized nitrogen-doped carbon quantum dots. *J. Phys. Chem. C* **2019**, *123*, 25570–25578. [CrossRef]
44. Ma, Y.; Sung, K.W.; Ahn, H.J. N- and F-co-doped carbon quantum dots coated on a Ni foam substrate as current collector for highly stable Li-air batteries. *Int. J. Energy Res.* **2023**, *2023*, 5310171. [CrossRef]
45. Jo, H.G.; Kim, K.H.; Ahn, H.J. Nitrogen-doped carbon quantum dots decorated on platinum catalysts for improved oxygen reduction reaction. *Appl. Surf. Sci.* **2021**, *554*, 149594. [CrossRef]
46. Gasidit, P.; Nagahiro, S.; Takahiro, I. Simple one-step synthesis of fluorine-doped carbon nanoparticles as potential alternative metal-free electrocatalysts for oxygen reduction reaction. *J. Mater. Chem. A* **2015**, *3*, 9972–9981.
47. Li, X.; Tang, Y.; Zhu, J.; Zhi, C.; Li, H. Boosting the cycling stability of aqueous flexible Zn batteries via F doping in nickel—Cobalt carbonate hydroxide cathode. *Small* **2020**, *16*, 2001935. [CrossRef] [PubMed]
48. Zhang, X.; Zhu, Y.; Chen, Y.; Dou, S.; Chen, X.; Dong, B.; Guo, B.; Liu, D.; Liu, C.; Chai, Y. Hydrogen evolution under large-current—Density based on fluorine-doped cobalt-iron phosphides. *Chem. Eng. J.* **2020**, *399*, 125831. [CrossRef]
49. Liu, M.X.; Gan, L.H.; Xiong, W.; Zhao, F.Q.; Fan, X.Z.; Zhu, D.Z.; Xu, Z.J.; Hao, Z.X.; Chen, L.W. Nickel-doped activated mesoporous carbon microspheres with partially graphitic structure for supercapacitors. *Energy Fuels* **2013**, *27*, 1168–1173. [CrossRef]
50. Lee, J.S.; Rajan, H.; Christy, M. Optimization of active sites by sulfurization of the core–shell ZIF 67@ZIF 8 for rapid oxygen reduction kinetics in acidic media. *Int. J. Hydrogen Energy* **2021**, *46*, 10739–10748. [CrossRef]
51. Sirisomboonchai, S.; Li, S.; Yoshida, A.; Guana, G. Terephthalic acid induced binder-free NiCoP-carbon nanocomposite for highly efficient electrocatalysis of hydrogen evolution eeaction. *Catal. Sci. Technol.* **2019**, *9*, 4651–4658. [CrossRef]
52. Lin, S.; Luo, J.; Xiao, C. Facile one-step synthesis of porous hybrid material fabricated by 2D nanosheets of molybdenum disulfide and reduced graphene oxide for efficient electrocatalytic hydrogen evolution. *Coord. Chem. Rev.* **2020**, *27*, 123–131. [CrossRef]
53. Liu, B.; Cao, B.; Cheng, Y.; Jing, P. Ultrafine CoP/Co_2P nanorods encapsulated in Janus/Twins-type honeycomb 3D nitrogen-doped carbon nanosheets for efficient hydrogen evolution. *iScience* **2020**, *23*, 101264. [CrossRef] [PubMed]
54. Ho, C.; Yilmaz, G.; Tan, C.F.; Hong, M. Functional defective metal-organic coordinated network of mesostructured nanoframes for enhanced electrocatalysis. *Adv. Funct. Mater.* **2018**, *28*, 1704177.
55. Thirukumaran, P.; Raji, A.; Shakila, A.; Madhappan, P. N-Doped mesoporous carbon prepared from a polybenzoxazine precursor for high performance supercapacitors. *Polymers* **2021**, *13*, 2048. [CrossRef]
56. Zhou, Z.H.; Zaman, W.; Sun, W.; Cao, L.; Tariq, M.; Yang, J. Cultivating crystal lattice distortion in IrO_2 via coupling with MnO_2 to boost the oxygen evolution reaction with high intrinsic activity. *Chem. Commun.* **2018**, *54*, 4959–4962. [CrossRef]
57. Pu, Z.; Cheng, R.; Zhao, J.; Hu, Z. Anion-modulated platinum for high-performance multifunctional electrocatalysis toward HER, HOR, and ORR. *iScience* **2020**, *23*, 101793. [CrossRef]
58. Ong, A.L.; Inglis, K.K.; Whelligan, D.K.; Murphy, S.; Varcoe, J.R. Effect of cationic molecules on the oxygen reduction reaction on fuel cell grade Pt/C (20 wt%) catalyst in potassium hydroxide (aq, 1 mol dm^{-3}). *Phys. Chem. Chem. Phys.* **2015**, *17*, 12135–12145. [CrossRef]
59. Choi, C.H.; Baldizzone, C.; Grote, J.P.; Schuppert, A.K.; Jaouen, F.; Mayrhofer, K. Stability of Fe_6N_6C catalysts in acidic medium studied by operando spectroscopy. *Angew. Chem. Int. Ed.* **2015**, *54*, 1275361275. [CrossRef]
60. Ding, W.; Li, L.; Xiong, K.; Wang, Y.; Li, W.; Nie, Y.; Chen, S.G.; Qi, X.Q.; Wei, Z.D. Shape fixing via salt recrystallization: A morphology-controlled approach to convert nanostructured polymer to carbon nanomaterial as a highly active catalyst for oxygen reduction reaction. *J. Am. Chem. Soc.* **2015**, *137*, 54146542. [CrossRef] [PubMed]
61. Chang, H.; Min, W.; Han, C.; Sung, H. N- and P, N-doped graphene as highly active catalysts for oxygen reduction reactions in acidic media. *J. Mater. Chem. A* **2013**, *1*, 3694–3699.
62. Lin, Q.P.; Bu, X.H.; Kong, A.G.; Mao, C.Y.; Bu, F.; Feng, P.Y. Heterometal-embedded organic conjugate frameworks from alternating monomeric iron and cobalt metalloporphyrins and their application in design of porous carbon catalysts. *Adv. Mater.* **2015**, *27*, 343163436. [CrossRef] [PubMed]
63. Karim, K. High efficiency platinum nanoparticles based on carbon quantum dot and its application for oxygen reduction reaction. *Int. J. Hydrogen Energy* **2017**, *42*, 11605–11613.

64. Muthusankar, G.; Sangili, A.; Chen, S.M.; Karkuzhali, R.; Sethupathi, M.; Gopu, G.; Karthicka, S.; Devi, R.; Sengottuvelan, N. In situ assembly of sulfur–doped carbon quantum dots surrounded iron (III) oxide nanocomposite; a novel electrocatalyst for highly sensitive detection of antipsychotic drug olanzapine. *J. Mol. Liq.* **2018**, *26*, 471–480. [CrossRef]
65. Martins, N.; Ângelo, J.; Girão, A.; Trindade, T.; Andrade, L.; Mendes, A. N–doped carbon quantum dots/TiO_2 composite with improved photocatalytic activity. *Int. J. Hydrogen Energy* **2016**, *193*, 67–74. [CrossRef]